

**Sum-of-harmonics method for improved narrowband and broadband signal  
quantification during passive monitoring of ultrasound therapies**

**Suggested Running Title:** A Sum-of-Harmonics narrowband and broadband filter

Erasmia Lyka<sup>a</sup>, Christian Coviello<sup>a</sup>, Richard Kozick<sup>b</sup>, Constantin-C. Coussios<sup>a)</sup>

<sup>a</sup> Institute of Biomedical Engineering, University of Oxford, Oxford OX3 7DQ,  
United Kingdom

<sup>b</sup> Department of Electrical and Computer Engineering, Bucknell University,  
Lewisburg, Pennsylvania 17837, USA

May 12, 2016

<sup>a)</sup> Author to whom correspondence should be addressed. Electronic email:  
constantin.coussios@eng.ox.ac.uk

**Abstract**

Passive Acoustic Mapping (PAM) enables real-time monitoring of ultrasound therapies by beamforming acoustic emissions emanating from the ultrasound focus. Reconstruction of the narrowband or broadband acoustic emissions component enables mapping of different physical phenomena, with narrowband emissions arising from non-linear propagation and scattering, non-inertial cavitation or tissue boiling, and broadband (generally, of significantly lower amplitude) indicating inertial cavitation. Currently, accurate classification of the received signals based on pre-defined frequency-domain comb filters cannot be guaranteed because varying levels of leakage occur as a function of signal amplitude and the choice of windowing function. This work presents a time-domain parametric model aimed at enabling accurate estimation of the amplitude of time-varying narrowband components in the presence of broadband signals. Conversely, the method makes it possible to recover a weak broadband signal in the presence of a dominant harmonic or other narrowband component. Compared to conventional comb filtering, the proposed sum-of-harmonics method enables PAM of cavitation sources that better reflect their physical location and extent.

PACS numbers: 43.60.Fg, 43.20.Fn, 43.25.Vt

## I. INTRODUCTION

### A) Monitoring of ultrasound therapies

Ultrasound has emerged over the last two decades as a non-invasive tool for a wide range of therapeutic applications, including tissue ablation and targeted drug delivery for cancer treatment, tissue fractionation (histotripsy) for tissue de-bulking or orthopedic applications, mechanical disruption of the blood-brain barrier and sonothrombolysis for stroke treatment (Coussios et al., 2007; Coussios and Roy, 2008; ter Haar, 2007; ter Haar and Coussios, 2007a, 2007b; Khokhlova et al., 2015; Liang et al., 2010; McDannold et al., 2008). The bio-effects associated with these different applications rely on thermal or mechanical mechanisms, or a combination of the two, which primarily arise from viscous absorption of the incident wave or the occurrence of acoustic cavitation in the ultrasound field (Coussios and Roy, 2008).

The wide clinical adoption of therapeutic ultrasound is hindered by the lack of an established, reliable monitoring technique that will provide real-time information on the progress and extent of the treatment. The currently clinically approved methods are B-mode imaging and MRI thermometry. B-mode imaging is a low-cost ultrasound method based on the principle of hyperechogenicity (Rabkin et al., 2005, 2006; Yu and Xu, 2008). Its main limitation though is its inability to monitor energy deposition unless boiling occurs or large bubble clouds are generated, as is the case in histotripsy, and the necessity to interlace it with the transmission of the therapeutic ultrasound pulse in order to avoid signal interference. MRI thermometry on the other hand is able to monitor temperature changes in three dimensions accurately (Graham et al., 1999; Quesson et al., 2000, 2011; Senneville et al., 2007), but its main

disadvantages are its high cost, limited temporal resolution and the fact that it cannot directly monitor cavitation activity.

Due to the limitations of the above methods, a different approach for monitoring cavitation-based ultrasound therapies has been introduced that is based on passively recording acoustic emissions originating from deep within the body where the therapeutic pulse is focused. In a typical clinical setup this method involves a transmitter of low or high power, with a single or multiple elements, responsible for transmitting the therapeutic pulse, and a single-element transducer or multiple-element array responsible for receiving acoustic emissions for monitoring purposes. These acoustic emissions could be classified according to their frequency domain signatures into narrowband and broadband. Narrowband signals correspond to harmonics, sub- or super-harmonics of the driving frequency of the therapeutic pulse, and they are mainly due to nonlinear propagation and scattering of the incident field, non-inertial cavitation or tissue boiling (Hamilton and Blackstock, 1998; Muir and Carstensen, 1980). On the other hand, inertial cavitation gives rise to emissions, which are very short in time, yielding broadband signals in the frequency domain. Depending on the application, the key underlying mechanism could be either inertial cavitation, as in case of drug delivery and tissue fractionation, or non-inertial cavitation in the case of sonothrombolysis or opening of the blood-brain barrier. Therefore, it is of great importance to robustly distinguish broadband and narrowband emissions and quantify the energy in each of these bands (Jensen et al., 2012).

Passive monitoring in a clinical setup involves certain challenges that need to be taken into consideration. Clinically available transmitters and receivers combined in a setup may have overlapping bandwidths, allowing the simultaneous recording of broadband, as well as narrowband emissions that are harmonics of the driving

frequency of the therapeutic pulse. The relative magnitude of narrowband to broadband emissions varies significantly depending on conditions such as the amplitude of the transmitted signal, the degree of tissue nonlinearity, the distance travelled by the transmitted acoustic wave until it is recorded, and the bandwidth of the receiver relative to the frequency of the transmitter. Therefore, an adaptive filtering method is required to accurately distinguish the frequency band of interest regardless of the relative magnitude of the simultaneously recorded interfering signal.

The most commonly experimentally used method is filtering in the frequency domain using a pre-defined comb filter (Choi and Coussios, 2012). However, the accuracy of this technique cannot be guaranteed due to the fixed characteristics (i.e. order, bandwidth, dB rejection, window function) of the comb filter. As the amplitude of the narrowband components of the signal that the comb filter aims to reject varies over time and across applications, the comb filter is unable to perform an equal rejection rate in the cases of lower and higher amplitude. More precisely, as the amplitude of a narrowband signal increases, a spreading of its energy is observed in the signal spectrum. Therefore, application of the same comb filter in different amplitude narrowband signals will result in partial removal of the energy of the narrowband signal, and thus distortion of the broadband component and misinterpretation of the broadband energy. The importance of acoustic signal filtration for the accurate quantification of the signal-of-interest has recently motivated several research groups. Two methods reported in the literature and demonstrating promising results are singular value decomposition (SVD) (Chitnis et al., 2015) and the discrete wavelet transform (Haqshenas and Saffari, 2015). The first one is based on the spectral signature of the eigenvectors calculated from the SVD analysis of beamformed RF data, while the second one decomposes the signal in its

frequency components by applying a series of filters with different cut-off frequencies at different scales.

An alternative method is proposed in this paper which is based on a time-domain data-adaptive parametric model for estimation of the narrowband component in a recorded signal, in the presence of interference and noise. The broadband component can be subsequently estimated by coherently subtracting the previously estimated narrowband signal from the recorded signal. This method allows estimation of all the components of the received signal, in contrast to comb filtering, which rejects the narrowband components in order to estimate the broadband one. A similar method has been used in modelling electrocardiograms as time-varying harmonic signals allowing the recovery of surface electromyographic signals (Zivanovic and Gonzalez-Izal, 2012).

## **B) Passive Acoustic Mapping**

Passive monitoring based on acoustic emissions recorded by a multi-element array is known as Passive Acoustic Mapping (PAM), and it is an ultrasound-based method that enables real-time monitoring of sources of nonlinear acoustic emissions. More specifically, the signals passively recorded from the channels of an array are independently filtered and then combined using either simple delay-and-sum or more sophisticated adaptive beamforming algorithms. The objective is to generate maps whose intensity at each location directly corresponds to the energy of the sources of acoustic emissions at the same location (Gyongy and Coussios, 2010; Gyöngy and Coussios, 2010; Jensen et al., 2012). Several beamforming algorithms for PAM have been reported in the literature. The initially proposed reconstruction method called

Time-Exposure Acoustics (TEA) is based on calculating the cross-correlation of the signals recorded by the individual elements of an array, which are pre-steered with respect to a specific location of interest. Although it has low computational cost, this algorithm does not provide adequate spatial resolution and it is susceptible to multi-bubble interference and variability in the sensitivity of individual array elements. Therefore, an alternative more complex data-adaptive algorithm, known as Robust Capon Beamformer (RCB) has been proposed for PAM (Coviello et al., 2015), providing better spatial resolution and rejection of multi-bubble interference, and dealing with array calibration uncertainties.

Since PAM is able to provide spatiotemporal monitoring of all nonlinear processes taking place during ultrasound-based therapies, it has already been shown to provide successful monitoring in a wide range of applications. For example, the ability to monitor tissue ablation during HIFU treatments using PAM compared to conventional B-mode imaging has already been demonstrated (Jensen et al., 2012). Passive acoustic maps of both broadband and harmonic emissions along with estimations of the heat deposition achieved during HIFU exposure provide a complete method for detection of the lesions' formation, mapping of the region of tissue ablation and estimation of the temperature rise in this region, in order to predict cell death and guide the HIFU treatment (Jensen et al., 2013; Khokhlova et al., 2006). In the field of drug delivery, it has been demonstrated that acoustic inertial cavitation is the key mechanism for enhanced delivery of drug-carrying vehicles and extravasation of the encapsulated anti-cancer drug (Arvanitis et al., 2011; Choi et al., 2014; Mo et al., 2012; Rifai et al., 2010). Therefore, PAM could be an effective way to monitor these acoustic emissions in real time and provide knowledge on the extent of drug delivery and release at the desired location. Studying the cavitation dynamics of

146 flowing microbubbles under different ultrasound exposure parameters is another field  
147 where PAM made a significant contribution by mapping the evolution of acoustic  
148 emissions in both space and time (Choi and Coussios, 2012). Promising results have  
149 also been demonstrated for the use of PAM to monitor the acoustic activity of  
150 microbubbles during transcranial focused ultrasound treatments aiming at  
151 sonothrombolysis or cavitation-induced blood-brain barrier disruption (Arvanitis et  
152 al., 2013; Jones et al., 2013; O'Reilly et al., 2014). Therefore, PAM, along with  
153 similar passive monitoring techniques (Haworth et al., 2012), is gaining increasing  
154 interest in monitoring ultrasound-based therapies.

155         Depending on the application, PAM must be able to monitor acoustic  
156 emissions related to different acoustic sources, and this necessitates accurate filtering  
157 of the recorded acoustic signals. The development of a reliable method for estimating  
158 the different components of the received signal that would replace the simplistic  
159 approach of comb filtering could bring PAM a step closer to clinical adoption, and  
160 this is the motivation for the method proposed in this paper. The paper is organized  
161 into five sections. Section II presents the Sum-of-Harmonics (SOH) model for the  
162 estimation of the narrowband and broadband components of the signal, along with a  
163 modified version to deal with the time-varying amplitude of the recorded signal. In  
164 Section III numerical simulation results regarding the parameters of the SOH model  
165 are presented. In Section IV the experimental setup for the evaluation of the  
166 performance of the SOH model and the corresponding results are presented and  
167 discussed, and finally, Section V contains a summary of the conclusions.



## II. THEORY

### A) Initial Sum-of-Harmonics (SOH) Model

As already mentioned, the channel data, i.e. the signals recorded passively by one or multiple sensors on an ultrasound array, are filtered as an initial signal processing step in order to distinguish the broadband and narrowband components. Assuming that the signal recorded by one sensor is  $y$ , it could be expressed as the sum of a broadband signal  $b$  and a harmonic (narrowband) signal  $h$  at each time sample  $n$ :

$$y[n] = h[n] + b[n] \Leftrightarrow Y = H + B \quad (1)$$

The vectors  $\mathbf{Y}$ ,  $\mathbf{H}$ , and  $\mathbf{B}$  contain the set of samples in a block of data with  $N$  samples.

Estimation of the harmonic component  $h$  will enable the estimation of the corresponding broadband component by coherently subtracting the harmonic component from the recorded signal.

$$b[n] = y[n] - h[n] \quad (2)$$

The broadband component is assumed to be white Gaussian noise, and the harmonic component is given by a deterministic parametric model. The harmonic component is modeled as a periodic signal consisting of a number  $q$  of sinusoidal harmonics (Whipps, 2003):

$$h[n] = \sum_{k=1}^q a_k \cos(k\omega_0 n + \varphi_k) = \sum_{k=1}^q u_k \cos(k\omega_0 n) + v_k \sin(k\omega_0 n) \Leftrightarrow$$

$$\Leftrightarrow \mathbf{H} = \mathbf{C}_q(\omega_0)\mathbf{u} + \mathbf{S}_q(\omega_0)\mathbf{v} \Leftrightarrow \mathbf{H} = \mathbf{W}_q(\omega_0)\mathbf{x} \quad (3)$$

where  $\omega_0 = 2\pi f_0 T$  is the driving frequency of the system and therefore the fundamental frequency of the narrowband component of the recorded signal,  $T$  is the sampling

period,  $n$  represents the time sample of the signal,  $a_i$  and  $\varphi_i$  are the amplitude and phase of the  $i^{\text{th}}$  harmonic, and  $u_i$  and  $v_i$  are the corresponding Cartesian amplitudes. The variable  $k$  that varies between 1 and  $q$  represents the number of narrowband components present in the received signal to be estimated by the model. In the case where only the harmonics of the driving frequency are to be estimated,  $k$  varies between 1 and  $q$  with an integer step equal to 1. However, fractional steps can also be used to estimate sub- and ultra-harmonics of the driving frequency. The second line in (3) is a matrix-vector formulation that is equivalent to the first line for a finite block of data with  $N$  samples, and the vector  $\mathbf{x}$  is a concatenation of the vectors  $\mathbf{u}$  and  $\mathbf{v}$ . The matrix  $\mathbf{W}_q(\omega_0)$  is a concatenation of the matrices  $\mathbf{C}_q(\omega_0)$  and  $\mathbf{S}_q(\omega_0)$ , where each of these matrices has dimension  $N \times q$ , with  $(n, k)$  elements  $\cos(k\omega_0 n)$  and  $\sin(k\omega_0 n)$ , respectively. The notation emphasizes that these matrices depend on the fundamental frequency  $\omega_0$  and the number of harmonics  $q$ .

The harmonic signal parameters that must be estimated from measured data are collected in a parameter vector  $\mathbf{P}$ :

$$\mathbf{P} = [\omega_0, u_1, u_2, \dots, u_q, v_1, v_2, \dots, v_q]^T = [\omega_0, \mathbf{x}]^T \quad (4)$$

Estimation of the parameters of the SOH signal is achieved using the Maximum Likelihood Estimation (MLE) method combined with a model order selection method (Lake, 1999; Myung, 2003). Assume for now that the fundamental frequency  $\omega_0$  and number of harmonics  $q$  are fixed. Then the observed signal  $\mathbf{Y}$  is a linear model with respect to parameter vector  $\mathbf{x}$  from (1) and (3). Since the broadband component  $\mathbf{B}$  is modeled as white Gaussian noise distributed as  $N(0, \sigma^2 \mathbf{I})$ , the probability density or likelihood function is

$$p(\mathbf{Y} | \omega_0, \mathbf{x}, \sigma^2) = \frac{1}{(2\pi\sigma^2)^{N/2}} \exp \left[ \frac{-1}{2\sigma^2} (\mathbf{Y} - \mathbf{W}_q(\omega_0)\mathbf{x})^T (\mathbf{Y} - \mathbf{W}_q(\omega_0)\mathbf{x}) \right] \quad (5)$$

215 The negative log-likelihood function  $J_q(\omega_0, \mathbf{x}, \sigma^2) = -\ln(p(\mathbf{Y} | \omega_0, \mathbf{x}, \sigma^2))$   
 216 has the following form after dropping terms that are independent of the parameters,

$$217 \quad J_q(\omega_0, \mathbf{x}, \sigma^2) = \left(\frac{N}{2}\right) \ln(\sigma^2) + \frac{1}{2\sigma^2} L_q(\omega_0, \mathbf{x}) \quad (6)$$

$$L_q(\omega_0, \mathbf{x}) = \|\mathbf{Y} - \mathbf{W}_q(\omega_0)\mathbf{x}\|^2$$

218 The maximum likelihood (ML) parameter estimates are the values that  
 219 maximize the likelihood function for an observed signal  $\mathbf{Y}$ , or equivalently minimize  
 220  $J_q(\omega_0, \mathbf{x}, \sigma^2)$ . The noise variance  $\sigma^2$  is an unknown parameter, so its ML estimate  
 221  $\widehat{\sigma^2} = (1/N)L_q(\omega_0, \mathbf{x})$  may be inserted into (6) to obtain the negative log-likelihood  
 222 that is concentrated with respect to the estimate of  $\sigma^2$ , yielding  $J_q(\omega_0, \mathbf{x}, \widehat{\sigma^2}) =$   
 223  $\left(\frac{N}{2}\right) \ln(L_q(\omega_0, \mathbf{x}))$ , where terms independent of the parameters are dropped. For  
 224 fixed  $\omega_0$  and  $q$ , the ML estimate of the parameter vector  $\mathbf{x}$  is as follows, along with the  
 225 negative log-likelihood function that is further concentrated with respect to the  
 226 estimate of  $\mathbf{x}$ :

$$227 \quad \widehat{\mathbf{x}} = \left(\mathbf{W}_q(\omega_0)^T \mathbf{W}_q(\omega_0)\right)^{-1} \mathbf{W}_q(\omega_0)^T \mathbf{Y} = \mathbf{W}_q(\omega_0)^+ \mathbf{Y}$$

$$228 \quad J_q(\omega_0, \widehat{\mathbf{x}}, \widehat{\sigma^2}) = \left(\frac{N}{2}\right) \ln(L_q(\omega_0, \widehat{\mathbf{x}})) = \left(\frac{N}{2}\right) \ln(\mathbf{Y}^T \boldsymbol{\Pi}_q^\perp(\omega_0) \mathbf{Y}) \quad (7)$$

229 where  $\mathbf{W}_q(\omega_0)^+$  is the pseudoinverse of  $\mathbf{W}_q(\omega_0)$ ,  $\boldsymbol{\Pi}_q(\omega_0) = \mathbf{W}_q(\omega_0)\mathbf{W}_q(\omega_0)^+$  is  
 230 the orthogonal projection matrix onto the column space of  $\mathbf{W}_q(\omega_0)$ , and  $\boldsymbol{\Pi}_q^\perp(\omega_0) =$   
 231  $\mathbf{I} - \boldsymbol{\Pi}_q(\omega_0)$  is the projection onto the orthogonal complement of the column space.  
 232 The MLE of the fundamental frequency for a fixed number of harmonics  $q$  is then the  
 233 value of  $\omega_0$  that minimizes the nonlinear least-squares cost function  $\mathbf{Y}^T \boldsymbol{\Pi}_q^\perp(\omega_0) \mathbf{Y}$ .  
 234 However, since  $q$  is not known, the number of harmonics and fundamental frequency  
 235 are estimated jointly by minimizing the Minimum Description Length (MDL)

criterion, which has the general structure  $J + \left(\frac{r}{2}\right) \ln(N)$ , where  $J$  is the negative log-likelihood and  $r$  is the number of parameters in the model. The number of SOH parameters is  $2q+1$  from (4), and using the negative log-likelihood in (7), the MDL criterion is (dropping terms that are independent of  $q$  and  $\omega_0$ )

$$\{\widehat{\omega}_0, \hat{q}\} = \arg \min_{\{\omega_0, q\}} \left\{ \left(\frac{N}{2}\right) \ln(\mathbf{Y}^T \boldsymbol{\Pi}_q^\perp(\omega_0) \mathbf{Y}) + q \ln N \right\} \quad (8)$$

Then these values are used to obtain the estimate of  $\mathbf{x}$  as  $\hat{\mathbf{x}} = \mathbf{W}_{\hat{q}}(\widehat{\omega}_0)^+ \mathbf{Y}$ , and then the SOH component of the data is estimated as  $\hat{\mathbf{H}} = \boldsymbol{\Pi}_{\hat{q}}(\widehat{\omega}_0) \mathbf{Y}$  and the broadband component is estimated as  $\hat{\mathbf{B}} = \mathbf{Y} - \hat{\mathbf{H}} = \boldsymbol{\Pi}_{\hat{q}}^\perp(\widehat{\omega}_0) \mathbf{Y}$ . Note that the estimated SOH and broadband components are orthogonal.

Further details on the SOH modelling and estimation approach are available in (Whipps, 2003), including computationally efficient methods for performing the joint minimization in (8).

## B) Modified Sum-of-Harmonics (SOH) Model

The initial SOH model is able to estimate constant amplitude for the  $i^{\text{th}}$  harmonic signal of frequency  $i\omega_0$ . In order to estimate a time-varying amplitude harmonic signal, the representation of the harmonic signal in (3) is modified:

$$h[n] = \sum_{k=1}^q u_k[n] \cos(k\omega_0 n) + v_k[n] \sin(k\omega_0 n) \quad (9)$$

As is observed from (9), the Cartesian amplitudes are functions of the sample index. The relationship between the Cartesian amplitudes,  $\mathbf{u}$  and  $\mathbf{v}$ , and the amplitudes and phases,  $\mathbf{a}$  and  $\boldsymbol{\phi}$ , of each harmonic signal present in the recorded signal is:

$$u_k[n] = -a_k[n] \sin \phi_k[n]$$

$$v_k[n] = a_k[n] \cos \varphi_k[n] \quad (10)$$

Now, by assuming that the amplitude parameters follow an  $m^{\text{th}}$  order polynomial function:

$$\begin{aligned} u_k[n] &= u_0^k + u_1^k n + u_2^k n^2 + \dots + u_m^k n^m \\ v_k[n] &= v_0^k + v_1^k n + v_2^k n^2 + \dots + v_m^k n^m \end{aligned} \quad (11)$$

the harmonic signal is written as:

$$\begin{aligned} h[n] &= \sum_{k=1}^q (u_0^k + u_1^k n + u_2^k n^2 + \dots + u_m^k n^m) \cos(k\omega_0 n) + (v_0^k + v_1^k n + v_2^k n^2 + \\ &\dots + v_m^k n^m) \sin(k\omega_0 n) \end{aligned} \quad (12)$$

The parameters to be estimated are, now:

$$\mathbf{P} = [\omega_0, u_i^1, u_i^2, \dots, u_i^q, v_i^1, v_i^2, \dots, v_i^q]^T \text{ for } i = 0:m \quad (13)$$

Equation (1) can be now written as:

$$\mathbf{Y} = \mathbf{W}_q \mathbf{x} + \mathbf{B} \text{ where } \mathbf{Y} \text{ is a } (N \times 1) \text{ vector of the recorded signal}$$

$$\mathbf{x} = [x_1, x_2, \dots, x_q]^T \text{ is a } ((2*m*q) \times 1) \text{ vector}$$

$$x_i = [u_0^i, u_1^i, u_2^i, \dots, u_m^i, v_0^i, v_1^i, v_2^i, \dots, v_m^i]^T \text{ is a } 2*(m+1) \times 1 \text{ vector}$$

$$\mathbf{W}_q = [W_c^1 W_s^1 W_c^2 W_s^2 \dots W_c^q W_s^q] \text{ is a } N \times 2*(m+1)*q \text{ matrix} \quad (14)$$

$$W_c^i = \begin{bmatrix} \cos(k\omega_0 n_1) & n_1 \cos(k\omega_0 n_1) & n_1^2 \cos(k\omega_0 n_1) & \dots & n_1^m \cos(k\omega_0 n_1) \\ \dots & \dots & \dots & \dots & \dots \\ \cos(k\omega_0 N) & N \cos(k\omega_0 N) & N^2 \cos(k\omega_0 N) & \dots & N^m \cos(k\omega_0 N) \end{bmatrix} \text{ is}$$

a  $N \times 2*(m+1)$  matrix

$$W_s^i = \begin{bmatrix} \sin(k\omega_0 n_1) & n_1 \sin(k\omega_0 n_1) & n_1^2 \sin(k\omega_0 n_1) & \dots & n_1^m \sin(k\omega_0 n_1) \\ \dots & \dots & \dots & \dots & \dots \\ \sin(k\omega_0 N) & N \sin(k\omega_0 N) & N^2 \sin(k\omega_0 N) & \dots & N^m \sin(k\omega_0 N) \end{bmatrix} \text{ is a}$$

$N \times 2^{*(m+1)}$  matrix

Following the steps of the Maximum Likelihood Estimation method combined with the MDL model order selection method described in part A of section II, and using the new expression for the matrix  $\mathbf{W}_q$ , estimates of both  $\omega_0$  and  $q$  are obtained. The only difference in this case is that the number of parameters  $r$  in the model is now  $2q(m+1)+1$  from (13), and using the negative log-likelihood function in (7), the MDL criterion is (dropping terms that are independent of  $q$  and  $\omega_0$ )

$$\{\hat{\omega}_0, \hat{q}\} = \arg \min_{\{\omega_0, q\}} \left\{ \left( \frac{N}{2} \right) \ln(\mathbf{Y}^T \boldsymbol{\Pi}_q^\perp(\omega_0) \mathbf{Y}) + q(m+1) \ln N \right\} \quad (15)$$

As soon as  $\omega_0$  and  $q$  are defined, the estimate of  $\mathbf{x}$  can be obtained by  $\hat{\mathbf{x}} = \mathbf{W}_{\hat{q}}(\hat{\omega}_0)^+ \mathbf{Y}$ , and then the SOH component of the data is estimated as  $\hat{\mathbf{H}} = \boldsymbol{\Pi}_{\hat{q}}(\hat{\omega}_0) \mathbf{Y}$  and the broadband component is estimated as  $\hat{\mathbf{B}} = \mathbf{Y} - \hat{\mathbf{H}} = \boldsymbol{\Pi}_{\hat{q}}^\perp(\hat{\omega}_0) \mathbf{Y}$ , as already presented in Section IIA.

Furthermore, it is expected that the estimation accuracy of random and varying-level fluctuations in the amplitude of each narrowband component of a signal using a polynomial function will decrease as the number of cycles in the signal increases. Therefore, it is proposed that the signal is segmented into several cycle parts and that the proposed method is applied independently on each part.

### III. NUMERICAL SIMULATIONS

An initial computational investigation was carried out in order to enable understanding of the relationship between the parameters of the model including the sampling frequency of the signal, the narrowband (harmonic)-to-broadband signal ratio, the number of cycles per segment, and the order of polynomial used to approximate the signal amplitude changes.

The input signal to these simulations comprises a fixed sum-of-harmonics signal and white Gaussian noise with variance  $\sigma^2$  that is chosen to set the harmonic to broadband ratio. The SOH signal  $h(t)$  consists of the first three harmonics of a sinusoid signal at  $f = 2\text{MHz}$ , described by the following equation

$$h(t) = (100 + A_1) \sin(2\pi ft) + (40 + A_2) \sin(2\pi(2f)t) + (20 + A_3) \sin(2\pi(3f)t) \quad (16)$$

where  $A_i$  is a time-varying amplitude distortion added to the fixed amplitude of each cycle for each frequency component of the sum-of-harmonics signal. This distortion is generated by normally distributed random samples (one for every cycle of the sum-of-harmonics signal) filtered with a narrowband bandpass filter, and it is amplified in order to be 12dB lower than the initial amplitude of each component. The second term of the input signal is the broadband component generated as white Gaussian noise, and its variance  $\sigma^2$  is chosen to provide a range of narrowband-to-broadband ratios (NBR) between 10 and 50dB. This component is meant to represent the emissions generated by inertially collapsing bubbles. These emissions are dependent on the second derivative of the volumetric change in the bubble, and inertial collapse will therefore invariably lead to a spectral signature that will appear as broadband over the bandwidth of the detecting transducer. For single bubbles, the broadband response can

be periodic, typically at subharmonics of the main excitation frequency, due to arrested collapses that result in period doubling and period tripling depending on the bubble size as dictated by the bifurcation diagram. However, in situations involving multiple (rather than single) bubbles and where the bubble size can be tightly controlled, the acoustic emissions arising from inertial collapses can be readily modelled as white Gaussian noise. Recent work enabling tight control of the initial bubble size to be sub-resonant and monodisperse, evidenced experimentally that inertial cavitation has an exclusively broadband signature modulated by the frequency response of the receiving transducer (Kwan et al., 2015a). These broadband acoustic emissions can be faithfully modelled as white Gaussian noise following deconvolution of the frequency response of the transducer.

The range of values for each of the parameters investigated in these simulations is summarized in Table 1:

**Table 1. Range of values of the set of parameters tested in the simulations.**

Parameter	Value range
Sampling Frequency	30 – 120MHz
Harmonic-to-Broadband ratio	10 – 50dB
Number of cycles per segment	4 – 40
Order of polynomial	0 – 5

Figure 1 demonstrates the effect that each of the parameters investigated has on the performance of the model. The mean-square-error (MSE) between the input



SOH signal and the estimate using the SOH model is used as a performance metric for the different parameter sets, and decrease in the MSE signifies performance improvement for the SOH model.

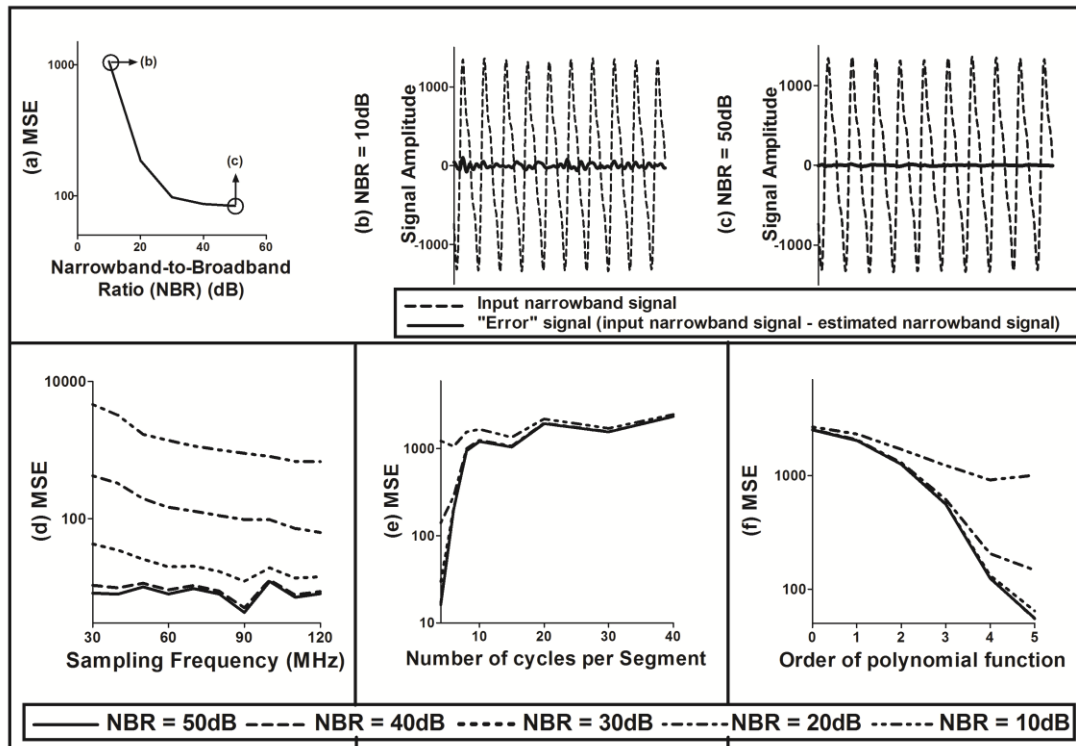


**Figure 1.** Simulation results for determining the effect of the parameters of the SOH model in its performance using mean-square-error (MSE) as a performance measure. The parameters evaluated are: (a) Narrowband-to-Broadband ratio (NBR) for sampling frequency = 82MHz, number of cycles per segment = 5, and order of polynomial = 2 (figures (b) and (c) demonstrate in the time domain a part of the input narrowband signal (dashed line), and the corresponding “error” signal (solid line) resulting from the subtraction of the estimated narrowband signal using the SOH model from the input narrowband signal), (d) Sampling frequency over a range of NBR (number of cycles per segment = 5, and order of polynomial = 2), (e) Number of cycles per segment over a range of NBR (sampling frequency = 82MHz, and order of polynomial = 2), and (f) Order of polynomial function over a range of NBR (sampling frequency = 82MHz, and number of cycles per segment = 5).

355           A significant improvement in the performance of the model is observed as the  
356 narrowband-to-broadband signal ratio (NBR) increases. This implies that estimation  
357 of a narrowband signal in the presence of a broadband component acting as  
358 interference is more accurate as the level of the interference decreases with respect to  
359 the level of the signal-of-interest. A small part of the generated narrowband signal is  
360 displayed in Fig.1b and 1c, along with the error signal between the generated and the  
361 estimated with the SOH model narrowband signal, for two NBR, demonstrating the  
362 level of the error in estimation in these two cases. With regards to the effect of the  
363 sampling frequency on the performance of the SOH model, it is observed that increase  
364 of the sampling frequency does not cause subsequent substantial decrease in the MSE.  
365 As far as the number of cycles per segment is concerned, it is observed that as this  
366 parameter decreases, better estimation of the narrowband component is achieved in  
367 the cases of high NBR. This could be explained by considering that when smaller  
368 signal segments are processed by the model, estimation of the signal amplitude  
369 fluctuations using a polynomial function is more accurate. However, when NBR is  
370 low, the performance of the model is decreased and the number of cycles per segment  
371 does not affect it substantially. Finally, evaluation of the effect of the order of the  
372 polynomial function chosen to represent changes in the amplitude of the narrowband  
373 signal has been performed. It is observed that in the cases of high NBR, as the  
374 polynomial order increases, the amplitude fluctuations are better fitted leading to  
375 decrease in the MSE.

#### IV. EXPERIMENTAL RESULTS

##### A) Experimental Setup

The experimental setup shown in Fig.2 aims to mimic clinical conditions that involve simultaneous generation of both narrowband (in this particular case harmonic) and broadband acoustic emissions. The goal is to evaluate the performance of the SOH model in classifying and quantifying broadband and narrowband components, when compared to conventional comb filters.

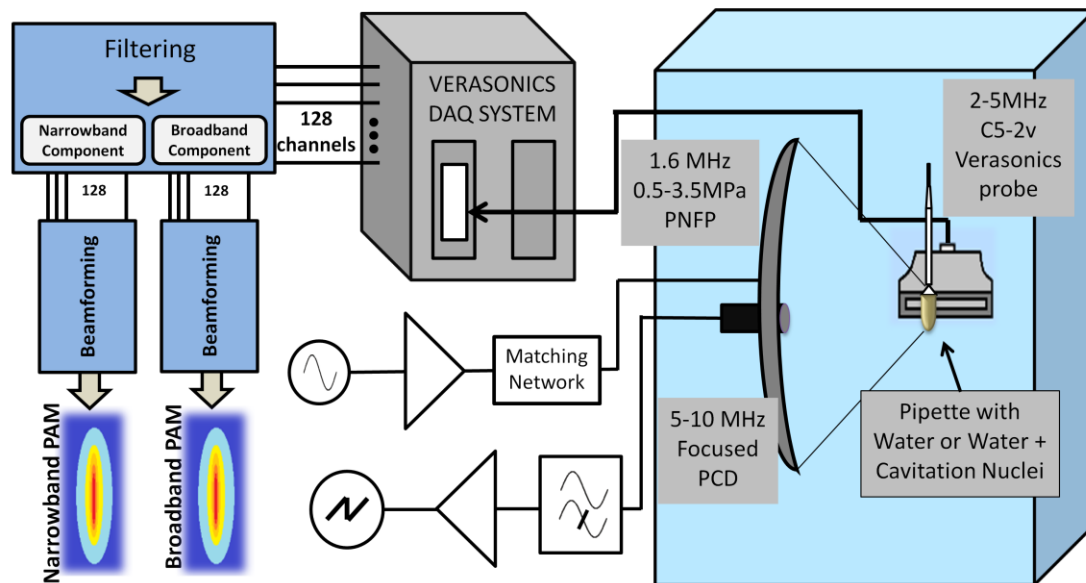


**Figure 2.**(Color online) Experimental setup involving a pasteur pipette filled with either water or cavitation nuclei is placed at the focus of a HIFU transducer driven at 1.6MHz. The HIFU transducer is co-aligned with a 5-10MHz PCD and a 2-5MHz array for B-mode imaging and passive recording of

acoustic emissions. These emissions are filtered, separating the harmonic and broadband component, which are then independently processed using PAM to provide separate maps of sources of harmonic and broadband emissions.

A 0.5MHz spherically focused, single-element ultrasound transducer (H-107D SN12; Sonic Concepts, Bothell, Washington, USA), with active diameter 64mm, focal length 62.6 mm, and a central, circular cut-out of diameter 22.6mm is placed in a large water tank of degassed, filtered water. It is co-aligned with a single-element spherically focused 7.5MHz transducer (aperture 12.5mm, focal length 75mm, Panametrics, Waltham, MA, USA), used as a passive cavitation detector (PCD), responsible for detecting the occurrence of inertial cavitation at the focal region. The HIFU transducer is connected to a function generator (33250A 30MHz function/arbitrary waveform generator, Agilent Technologies 2015), and it is driven at the 3<sup>rd</sup> harmonic (1.682MHz) transmitting a 1000-cycles sinusoid signal of increasing amplitude (0.5 – 3.5MPa), amplified by a 55dB power amplifier (1140LA, E&I, Rochester, NY, USA).

A Verasonics C5-2v convex array transducer (central frequency 3.5MHz, 128 elements, pitch 0.508mm, sensitivity -55.5 to -50.5dB, elevation focus 60mm, Verasonics, Inc. Redmond, WA) is placed perpendicular to the HIFU transducer with a plane of view that contains the focus of the HIFU transducer. The probe is connected to the Verasonics Vantage Research Ultrasound System (Verasonics, Inc. Redmont, WA), which is capable of simultaneously recording the signals received on each of the 128 channels of the array in order to enable generation of PAM maps.

A pasteur pipette is placed at the focus of the HIFU transducer and it is filled with either deionized water or a suspension of nanoparticles that act as cavitation nuclei; these nanoparticles are designed to lower the cavitation threshold of pure water to less than 2.5MPa at 1.682 MHz and enable sustained inertial cavitation activity within the sample volume (Kwan et al., 2015a, 2015b). The signal generated by the HIFU transducer propagates nonlinearly through the medium and it is reflected by the walls of the pipette. At the same time, inertial cavitation is expected to take place within the pipette above a certain amplitude threshold that depends primarily on the content of the pipette. Therefore, harmonic acoustic emissions due to nonlinear propagation and scattering, and broadband acoustic emissions due to inertial cavitation are simultaneously generated and passively recorded by the imaging probe.

#### B) Signal Filtering

The goal of this experiment is to process the recorded signals with either the proposed SOH model or a fixed comb filter, and quantify and compare the recovery of the two signal components for the two methods. Because either method of filtration should be implementable as part of a system for real-time monitoring of ultrasound therapies, only causal methods of filtration are used to benchmark the performance of the SOH model.

In the case of comb filtering, filters have been designed using the DSP toolbox of MATLAB. They are meant to attenuate the frequencies that are multiples of the driving frequency of the HIFU transducer. More specifically, they are IIR Butterworth filters of order 11, sampling frequency equal to 17.8MHz, they comprise of 6 notches in the frequency range of 0 to 8.1MHz, and their bandwidth is 0.5MHz, 1MHz, and 1.5MHz respectively. The selection of the order of the comb filters has been based on

two factors: the ability of the filter to remove the narrowband (harmonic) components effectively without affecting the broadband component, and the time required for filtering, since the goal is to implement a real-time system for passive acoustic mapping.

Regarding the SOH model, the recorded signal has been segmented into 8 cycles, and a 3<sup>rd</sup> order polynomial function has been chosen to represent the variations in the amplitude of the narrowband signal. The selection of the above parameters has been based on our simulation results, providing us with a satisfying filter performance and the ability to be performed in real-time.

#### **No cavitation nuclei**

At this stage of the experiment, no inertial cavitation is expected to take place in the pipette for the range of pressures induced at the HIFU focus. This hypothesis is supported by analyzing the signal from the middle channel of the array, and observing no change in its variance with increasing peak rarefactional pressure amplitude.

Based on this assumption, the broadband component of the recorded signal in each channel of the array should correspond to the baseline noise of the system at each pressure. The baseline noise of the system is measured at each pressure using the setup in Fig.2, when there is no pipette placed at the focal region. By removing the harmonic components from the signal recorded from the middle (64<sup>th</sup>) channel of the array using either the proposed SOH model or a comb filter, the power of the remaining signal, i.e. the power of the broadband component, should be very close to the power of the baseline noise at each pressure.

459           In order to choose optimal parameters for the comb filters, the power of the  
460 broadband component has been calculated for four different comb filters of the same  
461 bandwidth (1.5MHz) and different order, and it is presented along with the power of  
462 the baseline noise in Fig.3 for the range of pressures tried in the experiment. It is  
463 expected that as the filter order increases, the peaks of the filter become sharper,  
464 providing at the same time higher narrowband signal rejection, as observed by the  
465 magnitude response of the filters. This means conceptually that the harmonics are  
466 more effectively attenuated, but the frequency range surrounding the harmonics  
467 becomes more readily attenuated too. Therefore, depending on the order selected  
468 there is a trade-off between harmonic rejection efficiency and unwanted broadband  
469 signal rejection (signal-of-interest remaining unaffected). In Fig.3 it is demonstrated  
470 that as the order of the filter increases the calculated broadband power decreases, but  
471 after a certain point it reaches a plateau. At the same time, as the pressure increases  
472 the broadband power for all the comb filters still increases, signifying that there is still  
473 some harmonic energy remaining after filtering, and the decrease in the power for  
474 increasing filter order could not only be due to better harmonic rejection but also due  
475 to part of the broadband energy being erroneously filtered out. It is therefore, believed  
476 that comb filter of order 11 performs adequately, as the broadband power calculated is  
477 close to the baseline noise, providing a satisfying compromise between harmonic  
478 rejection and preservation of the signal-of-interest. Furthermore, increase of the order  
479 of the filter has a significant impact on the computational cost of filtering. Since the  
480 goal is to enable real-time PAM, an 11<sup>th</sup> order filter was thus chosen as it enables  
481 generation of passive acoustic maps at a frame rate comparable to SOH, namely  
482 approximately 3Hz (main computer specifications: Intel Xeon CPU E2-2650 v2,  
483 32GB RAM, NVIDIA GeForce GTX TITAN Black GPU).

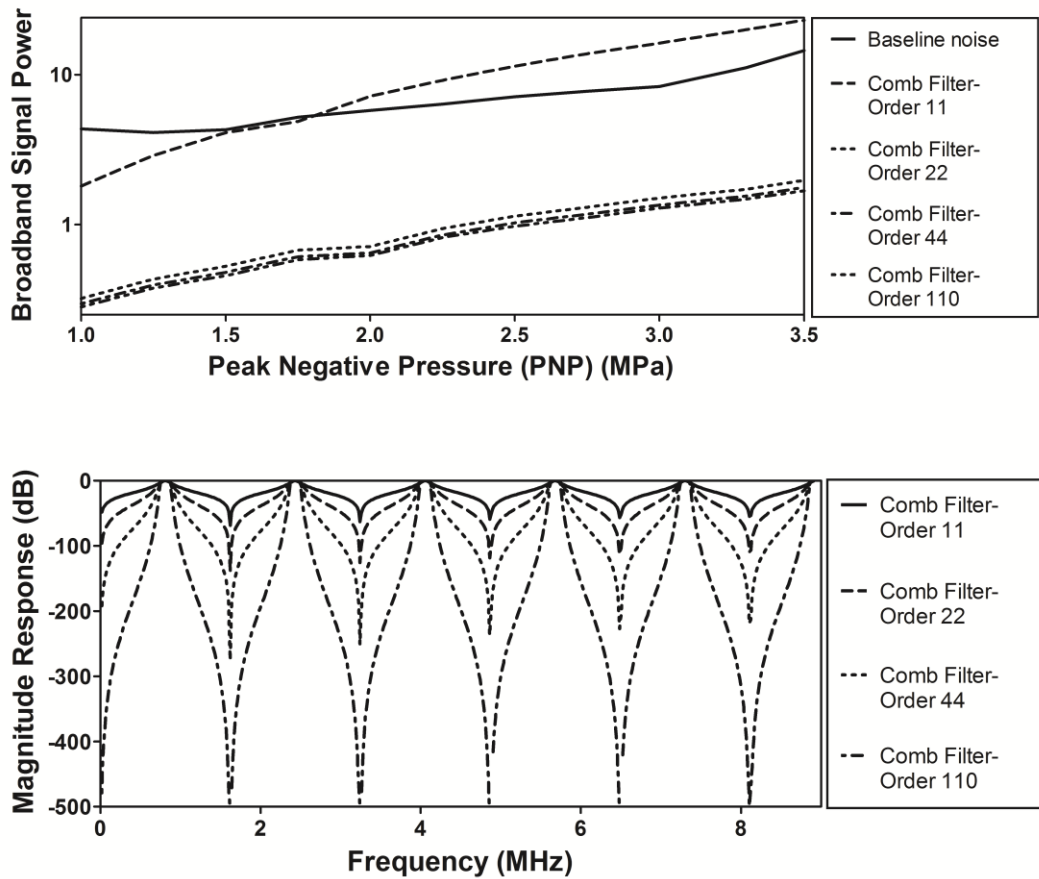


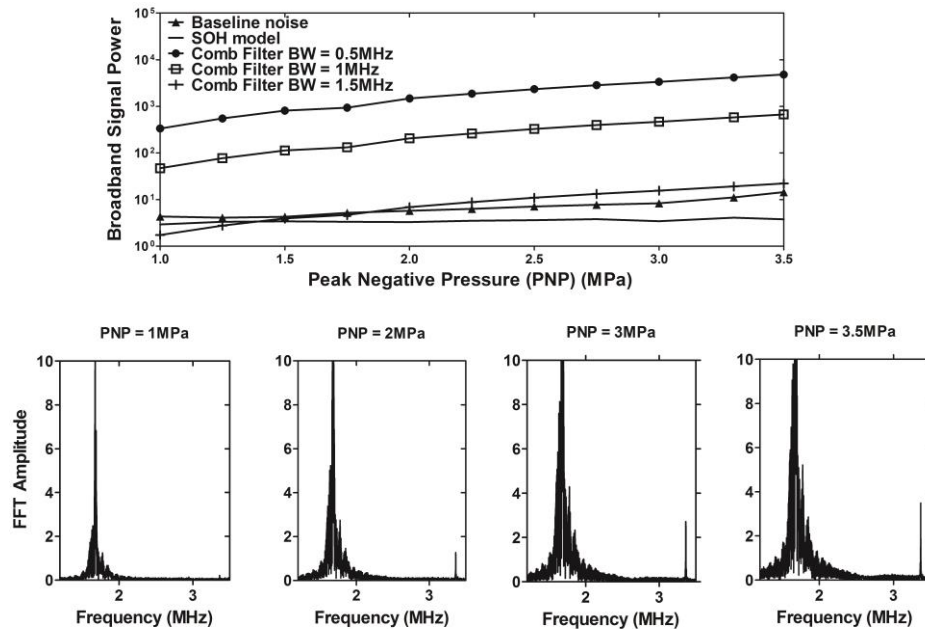
**Figure 3.** Power of the broadband component of the signal recorded at the 64<sup>th</sup> channel of the array, when water is placed in the pipette, for the range of peak negative pressures tested in the experiment, when the harmonic components are filtered out using a comb filter of 1.5MHz bandwidth and order equal to 11, 22, 44 or 110. The power of the baseline noise corresponds to the recorded signal when nothing is placed at the focus. The magnitude response of the different comb filters with respect to frequency is displayed in the lower part of the figure.

By selecting the order of the three comb filters to be equal to 11, the only parameter allowed to vary amongst them is the bandwidth. In Fig.4 the power of the broadband component corresponding to the 64<sup>th</sup> channel (central element) of the array is presented after filtering of the narrowband components using either the SOH model or one of the fixed-order (11<sup>th</sup> order), varying bandwidth (0.5MHz, 1MHz and



497 1.5MHz) comb filters. It is observed that as the bandwidth of the comb filter  
498 increases, its performance is improved, and the power of the broadband component  
499 approaches the power of the baseline noise. For the ideal filter, the broadband power  
500 should remain constant across all ultrasound pressure amplitudes in the absence of  
501 cavitation. The broadband power should thus remain unaffected by changes in the  
502 narrowband-to-broadband ratio, whilst at the same time being no greater than the  
503 baseline noise power. The only filter that satisfies these criteria is the SOH model,  
504 which can therefore be deemed to outperform the chosen comb filters. On the  
505 contrary, when the signal is filtered using a comb filter, an increase in the power of  
506 the broadband component is observed as pressure increases. By studying the spectra  
507 of the recorded signal at different pressures, a leakage of harmonic energy is observed  
508 at a wider frequency band. As a consequence, application of the same fixed comb  
509 filter at a signal of increasing pressure will result in increased harmonic power not  
510 being efficiently filtered out. This power will be misinterpreted as broadband power,  
511 and as is expected, it increases as the pressures increases. At the same time, as the  
512 bandwidth of the filter widens, the filter is also attenuating part of the broadband  
513 component. The above two observations combined could potentially explain the lower  
514 power, compared to baseline broadband power, obtained for weak excitation pressures  
515 in the case of the wide comb filter. More specifically, at low pressures the narrowband  
516 components are more effectively filtered out, but at the same time part of the  
517 broadband component is also filtered out, leading to decreased estimated broadband  
518 power. As the pressure increases, filtering of part of the broadband signal still takes  
519 place, but the leakage of harmonic energy from the filter increases. The harmonic  
520 components remaining in the signal as pressure increases are higher compared to the

521 broadband component falsely filtered out, and as a consequence the estimated  
 522 broadband power increases.



523

524 **Figure 4.**Power of the broadband component of the signal recorded at the 64<sup>th</sup> channel of the array,  
 525 when water is placed in the pipette, for the range of peak negative pressures tested in the experiment,  
 526 when the harmonic components are filtered out using either one of the chosen comb filters or the SOH  
 527 model. The power of the baseline noise corresponds to the recorded signal when nothing is placed at  
 528 the focus. The spectrum of the totally recorded signal from the 64<sup>th</sup> channel of the array is displayed in  
 529 the lower part of the figure at four different pressures (1, 2, 3, and 3.5MPa) that cover the whole range  
 530 of pressures evaluated.

531

## 532 **With cavitation nuclei**

533 By replacing the water-filled pipette with a pipette containing a suspension of  
 534 cavitation nuclei it is expected that above a certain pressure threshold, inertial  
 535 cavitation will occur. In Fig.5 the spectrum of the PCD data, as well as the spectrum  
 536 of the signal recorded by the 64<sup>th</sup> channel of the array, is displayed over the range of

pressures tested in the experiment. In both sets of figures, it is observed that there is a significant increase in the level of broadband noise between 2 and 3MPa, indicating that the inertial cavitation threshold of the cavitation nuclei used in this experiment at 1.6MHz is between 2MPa and 3MPa.

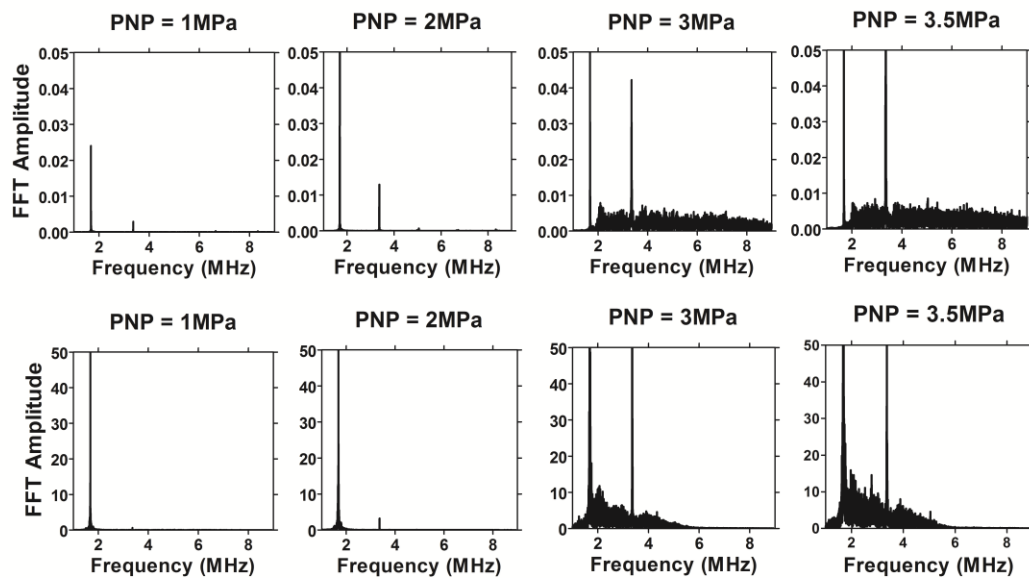


**Figure 5.** The spectrum of the PCD data (top) and the signal recorded at the middle (64<sup>th</sup>) channel of the array (bottom) is displayed, for four different pressures (1, 2, 3, and 3.5MPa) covering the range of pressures tested in the experiment, when cavitation nuclei are placed in the pipette.

In order to further establish the conclusions from Fig.4 regarding the efficiency of the SOH model in rejecting the narrowband component while preserving the broadband component, Fig.6 is introduced. In this figure the spectrum of the signal recorded from the middle (64<sup>th</sup>) element of the array, and the spectra of the broadband component of the recorded signal after being filtered with either the SOH model, the wide or the narrow comb filter are presented. The SOH model is able to remove the narrowband signal component effectively with minimal impact on the

broadband signal component. By contrast, the narrow comb filter fails to remove all of the narrowband peak, and the wide comb filter removes much of the broadband signal surrounding the peak, resulting in misclassification of part of the broadband energy as narrowband.

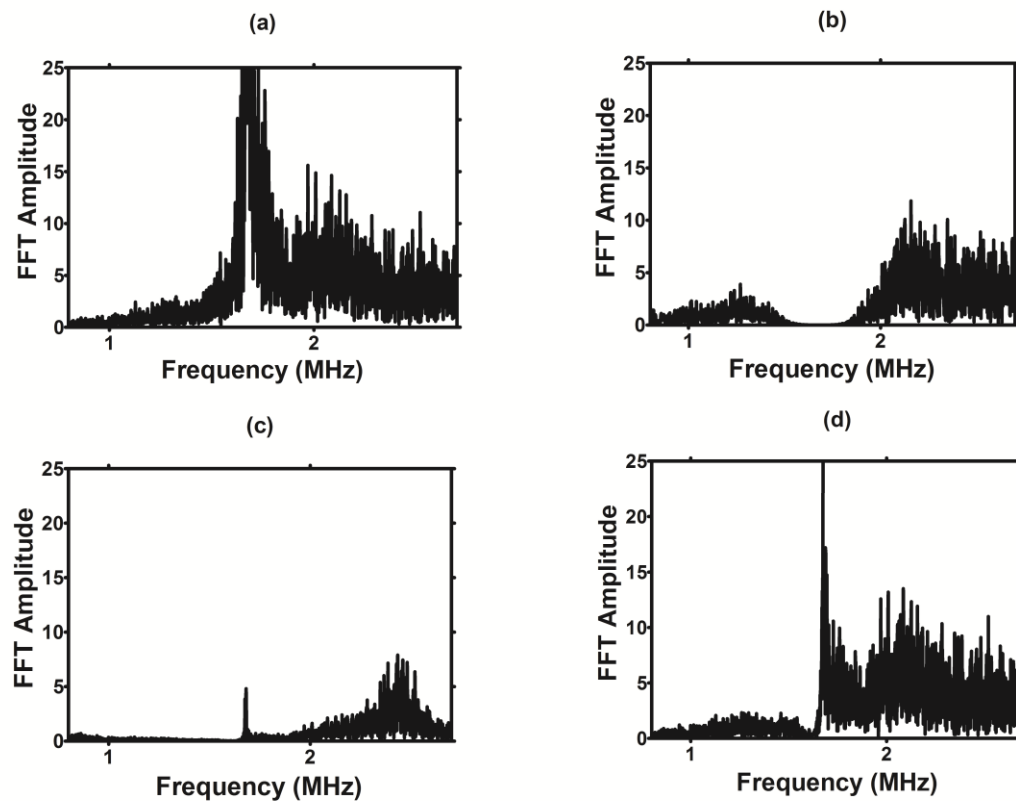


**Figure 6.** Frequency spectrum of (a) the recorded unfiltered signal from the middle (64<sup>th</sup>) channel of the array at 3.5MPa in the presence of cavitation nuclei, filtered with (b) the SOH model, (c) a wide bandwidth comb filter (order = 11, sampling frequency = 17.8MHz, bandwidth = 1.5MHz), and (d) a narrow bandwidth comb filter (order = 11, sampling frequency = 17.8MHz, bandwidth = 1.5MHz).

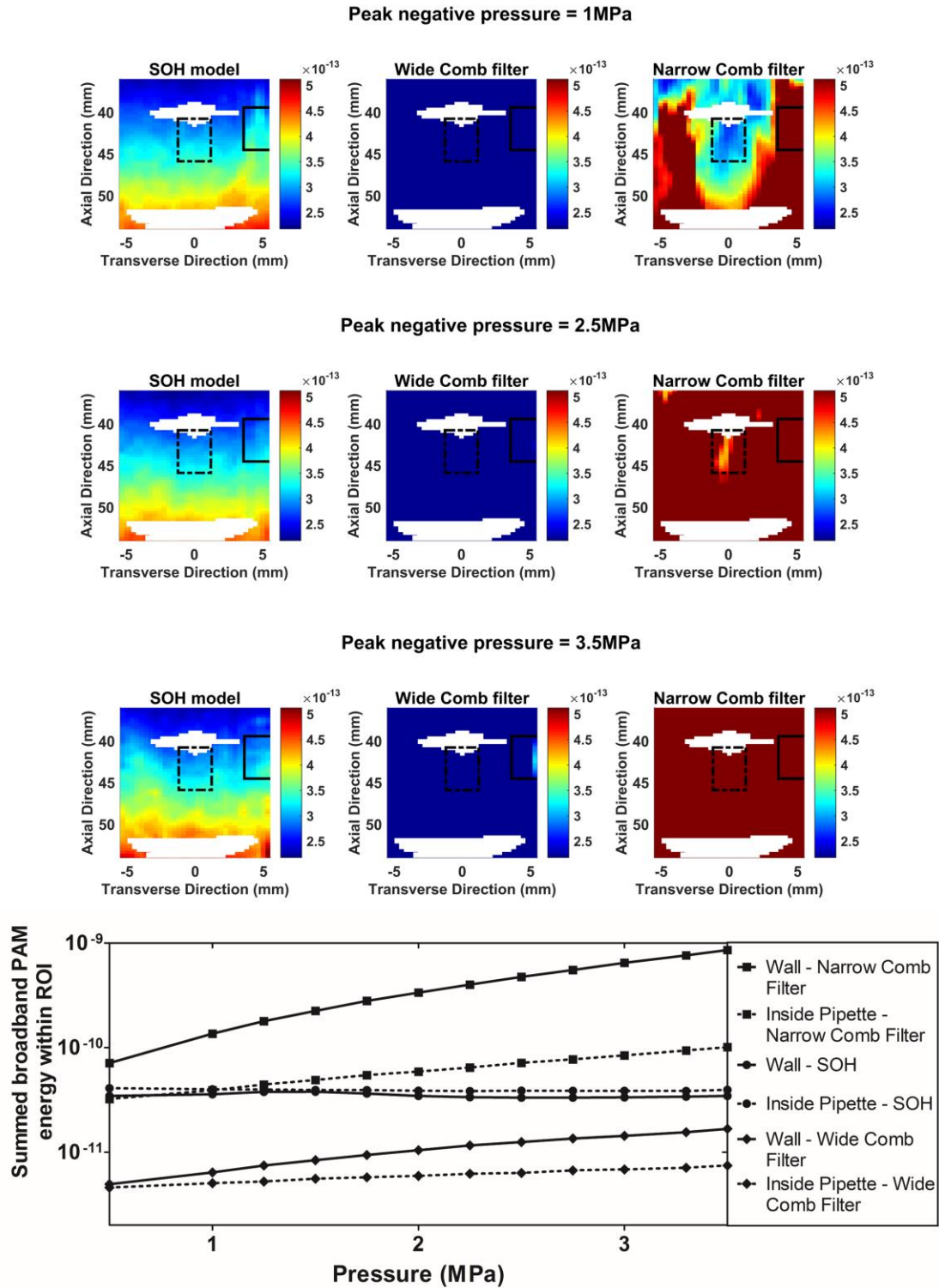
### C) Passive Acoustic Mapping

The second aim of the experiment is to evaluate the effect of the filtering method on the spatial accuracy of PAM maps. Particular attention is placed on the capability of each method to remove interference from strong harmonic reflections

from the pipette walls. Passive acoustic maps of inertial cavitation are generated for the broadband component of data filtered using either the SOH or comb-filter method and applying the RCB beamforming algorithm, with the factor  $\varepsilon$  being equal to 6. The optimal value of epsilon is data-dependent, and the selection of this value is based on a trade-off between optimal interference suppression and optimal energy estimation (Coviello et al., 2015). During the experiments presented in this section, the same data sets have been processed with either the SOH model or the comb filters, and in both cases the same value of epsilon has been used to generate PAM maps. Therefore, the comparison of the filtering techniques in the context of PAM is not affected by the selection of the value of epsilon.

#### **No cavitation nuclei**

Since no inertial cavitation takes place in the pipette, the generated maps should display no activity. In Fig.7 the maps corresponding to all filtering techniques are displayed, using the same linear color scale, at three different pressures (1MPa, 2.5MPa, and 3.5MPa). The white areas displayed on the PAM maps signify the locations of the walls of the pipette, as these appear on the B-mode images recorded, after a -6dB power threshold is applied. The minimum and maximum value in the colormap is the minimum and maximum PAM power respectively calculated in the case of the SOH model for all excitation pressure amplitudes tested in this part of the experiment.



587

588 **Figure 7.**(Color online) PAM maps of sources of broadband acoustic emissions, when water is placed  
 589 in the pipette, are displayed at three different pressures: 1MPa, 2.5MPa, and 3.5MPa. The white areas  
 590 displayed signify the reflections from the two walls of the pipette, as they appear on B-mode images  
 591 after a -6dB power threshold is applied. The broadband component is determined by filtering the

received acoustic emissions with either the SOH model (left maps), a wide bandwidth (order = 11, sampling frequency = 17.8MHz, bandwidth = 1.5MHz) (middle maps) or a narrower bandwidth (order = 11, sampling frequency = 17.8MHz, bandwidth = 0.5MHz) (right maps) comb filter. The colormap used for all the subfigures is defined by the minimum and maximum PAM power calculated in the case of the SOH model among all pressures tested in the experiment. Two ROI have been defined in the PAM maps, one on the vertical walls of the pipette with respect to the array, and one in the middle of the pipette. The summed PAM power in each of these regions is displayed in the lower part of the figure for the case of the SOH model and the two comb filters over the range of pressures tested in the experiment.

As the pressure increases, the maps corresponding to the SOH model remain unchanged and no activity is observed, as is expected. However, in the cases of the narrow comb filter significant activity is observed in the maps, even at the lowest pressure, falsely indicating that inertial cavitation takes place. Therefore, it is safe to conclude that the mapped activity corresponds to harmonic energy that is not properly filtered out. In the case of the wide bandwidth comb filter, which according to our previous results performs better than the other comb filters, it is observed that some activity is mapped at the regions where the vertical (with respect to the array) boundaries of the pipette exist. Since strong harmonic reflections of the incident wave are expected by these interfaces, this enhances the previous conclusion regarding high-level harmonic emissions not efficiently being filtered out and therefore, misinterpreted as broadband. At this point it is important to explain the increase in PAM power with respect to depth observed in the case of the SOH model for all pressures. The signal mapped in these figures is the electrical background noise of the system, since no cavitation takes place. As part of the PAM algorithm, signal amplitude compensation for spherical spreading of the recorded acoustic emissions

takes place. But since noise is independent of distance from the array, spherical spreading compensation of the noise signal will result in the increase of the noise contribution with respect to distance. This phenomenon is not observed in the PAM maps corresponding to the two comb filters due to the use of the same colormap for all filters, although the signal amplitudes mapped are considerably different.

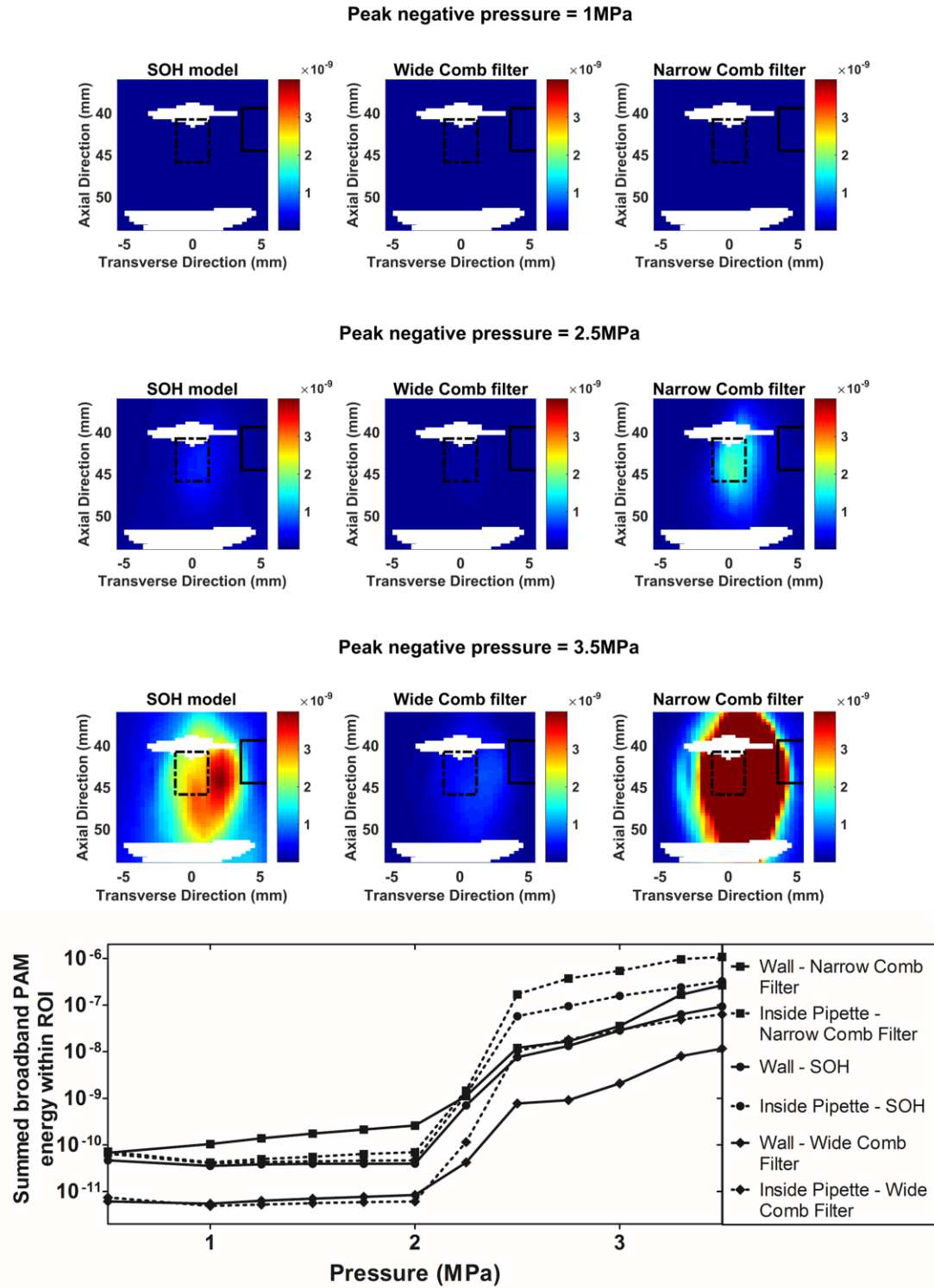
The above conclusions could be further enhanced by selecting regions of interest (ROI) in the PAM maps and comparing the summed PAM power within these regions. Two regions have been selected in our case, one at the vertical (with respect to the array) boundaries of the pipette, and one in the middle of the pipette, as demonstrated in Fig.7. Regarding the SOH model, the summed power in both regions is fairly equal, as is expected, since in this case the broadband component mapped corresponds only to the background noise of the system. It also remains stable regardless of the increase in the pressure, indicating that all the harmonic components have been efficiently removed at all pressures. On the other hand, in the case of the comb filters, the summed power from both regions increases as the pressure increases, indicating that part of the harmonic component has not been filtered out. This effect is mainly apparent in the region near the walls of the pipette, but it is also observable in the region in the middle of the pipette mainly due to a combination of the point-spread function of the PAM method and reflections from the horizontal boundaries of the pipette.

#### **With cavitation nuclei**

The goal of this part of the experiment is to evaluate the spatial accuracy of mapping inertial cavitation using the SOH model as a filtering technique compared to comb filtering. Similar to the previous stage of the experiment, PAM maps are



643 generated using the broadband component of the recorded signals from the array, and  
644 displayed in Fig.8 for three different pressures (1MPa, 2.5MPa, and 3.5MPa) with the  
645 same linear color scale. The colormap in the sub-figures of Fig.8 is defined according  
646 to the minimum and maximum value of PAM power calculated for the case of the  
647 SOH model among all pressures tried in this part of the experiment. The white areas  
648 displayed on the PAM maps signify the locations of the walls of the pipette, as these  
649 appear on the B-mode images recorded, after a -6dB power threshold is applied.



650

651 **Figure 8.**(Color online) PAM maps of sources of broadband acoustic emissions, when cavitation nuclei  
 652 are placed in the pipette, are displayed at three different pressures: 1MPa, 2.5MPa, and 3.5MPa. The  
 653 white areas displayed signify the reflections from the two walls of the pipette, as they appear on B-  
 654 mode images after a -6dB power threshold is applied. The broadband component is determined by

655 filtering the received acoustic emissions with either the SOH model (left maps), a wide bandwidth  
656 (order = 11, sampling frequency = 17.8MHz, bandwidth = 1.5MHz) (middle maps) or a narrower  
657 bandwidth (order = 11, sampling frequency = 17.8MHz, bandwidth = 0.5MHz) (right maps) comb  
658 filter. The colormap used for all the subfigures is defined by the minimum and maximum PAM power  
659 calculated in the case of the SOH model among all pressures tested in the experiment. Two ROI have  
660 been defined in the PAM maps, one on the vertical walls of the pipette with respect to the array, and  
661 one in the middle of the pipette. The summed PAM power in each of these regions is displayed in the  
662 lower part of the figure for the case of the SOH model and the two comb filters over the range of  
663 pressures tested in the experiment.

664

665 At the lowest pressure displayed, which is below the cavitation threshold  
666 identified, no inertial cavitation is observed. As the pressure increases and exceeds the  
667 cavitation threshold, inertial cavitation activity is more apparent in the case of the  
668 SOH model and the narrow comb filter, being significantly more extensive in the case  
669 of the narrow comb filter. This observation is consistent with the previously shown  
670 results, since overestimation of inertial cavitation is expected due to a significant part  
671 of the harmonic signal not being efficiently removed. In the case of the wide comb  
672 filter, inertial cavitation activity at the cavitation threshold is barely observable.  
673 Finally, at the highest pressure tested significant inertial cavitation activity is observed  
674 in all three cases, and in the case of the SOH model this activity is mapped within the  
675 expected physical area defined by the boundaries of the pipette, compared to the case  
676 of the narrow comb filter, where inertial cavitation seems to happen outside the walls  
677 of the pipette, which is not physically possible in the context of the present  
678 experimental setup. As far as the wide comb filter is concerned, although inertial  
679 cavitation is mapped within the expected physical boundaries, its intensity is lower  
680 than that of the SOH model. This could be explained by considering the effect that the

wide comb filter has on the recorded signal in the case where inertial cavitation takes place. Due to its wide bandwidth, it removes a significant part, but not the whole, of the harmonic energy, as was already demonstrated, and simultaneously a part of the broadband energy (Fig.6). Therefore, it could lead to underestimation of the intensity and extent of inertial cavitation and potentially cause the onset of inertial cavitation activity to be missed, as was observed in the PAM maps in Fig.8 at 2.5MPa. Finally, by studying the same ROI as in the case where no cavitation nuclei are in the pipette, the same conclusions as above could be drawn. More specifically, the summed PAM power in the ROI at the middle of the pipette is suddenly increasing for all the filters between 2 and 3MPa, where the cavitation threshold is expected. The main difference lies on the fact that before this threshold is exceeded only the SOH model is able to completely remove the narrowband components, indicated by the constant power calculated, while for the comb filters PAM power increases with pressure, as has already been discussed. Regarding the ROI on the wall of the pipette, it is interesting to point out the increase in the summed PAM power for both the SOH model and the comb filters as soon as the cavitation threshold is exceeded. This could be justified by considering the combination of the following two parameters: inertial cavitation taking place near or at the wall of the pipette, and the effect of the point-spread function of the PAM method.

## V. CONCLUSIONS

A data-adaptive method has been proposed in this paper for the estimation of the narrowband component in a narrowband-plus-broadband signal. The SOH model

has been proven to be effective in estimating the parameters required to define a narrowband signal using an optimization method. Coherently subtracting the estimated narrowband signal from the recorded signal provides an accurate estimate of its broadband component. All analysis in the present work was performed using time-domain filters, however it is possible that notch filters in the frequency domain could minimize inappropriate inclusion or rejection of spectral leakage (O'Reilly and Hynynen 2012, Salgaonkar et al 2009). However, such frequency-domain filters would need to be adjusted based on the pulse duration and windowing applied, whereas the sum-of-harmonics model automatically accounts for pulse duration and windowing effects irrespective of the amplitude of the original signal.

According to our simulations, the proposed method is able to provide an accurate estimation of the narrowband signal component, especially in cases of high NBR. This is a significant advance in the context of clinical applications, where weak broadband signals arising from inertial cavitation need to be distinguished from elevated harmonic signals arising from strongly reflecting structures such as bone.

Splitting the received signal into sub-parts including a small number of cycles prior to processing has been shown to yield further improvements in narrowband signal estimation. A first level of parallelization of the method could be implemented at this point, since estimation of the necessary parameters in each signal part is independent, moving the method one step closer to real-time execution. It is also worth mentioning that the computational complexity of our method is on the order of  $O(N^3)$ , while the computational complexity of the comb filtering method is lower, on the order of  $O(N \log(N))$ , where  $N$  is the data size. However, the selection of the appropriate hardware, along with a multiple-level parallelized implementation of the model on the cores of a GPU is expected to achieve real-time performance of the

algorithm. Finally, it is important to point out that the selection of the order of the polynomial function used to approximate the changes in signal amplitude plays a significant role in the performance of the model. However, increased accuracy comes at the expense of increased computation.

Our in-vitro experiments allowed us to investigate the impact of improved filtration on the spatial accuracy of PAM. More specifically, the SOH model enabled accurate estimation of the amplitude of time-varying narrowband components, recovering, as a consequence a weak broadband signal. Furthermore, it enables the generation of PAM maps of inertial cavitation activity that spatially coincide with the physical area within which cavitation nuclei can exist. By contrast, PAM maps obtained using conventional comb filtration could erroneously indicate the occurrence of inertial cavitation activity several mm beyond the physical boundaries within which cavitation can exist (narrowband comb filters), or significantly underestimate the intensity and extent of inertial cavitation activity leading to misinterpretation of the onset of inertial cavitation (wideband comb filters). We can therefore speculate that PAM maps generated using the SOH model are more likely to accurately describe the location, intensity and extent of the different ultrasound bio-effects associated with narrowband or broadband acoustic sources, such as opening of the blood brain barrier or drug release.

In conclusion, the proposed SOH method is expected to enable significant improvements in the spatial accuracy of PAM as a tool for real-time monitoring of ultrasound therapies. The proposed method could also find application in conventional active ultrasound imaging or other acoustic signal processing requiring separation of a low-amplitude broadband signal from a high-amplitude narrowband component, or vice versa.

755

756

## VI. ACKNOWLEDGEMENTS

757

758

759

760

The authors gratefully acknowledge financial support from the UK's Engineering and Physical Sciences Research Council (EPSRC) under Programme Grant EP/K021729/1 (ULTRASPINE: Ultrasound-Enabled Minimally Invasive Disc Replacement), and EPSRC Departmental (DTA) Studentship (E.Lyka).

761

## VII. REFERENCES

762

763

764

Arvanitis, C. D., Bazan-Peregrino, M., Rifai, B., Seymour, L. W., and Coussios, C. C. (2011). "Cavitation-Enhanced Extravasation for Drug Delivery," *Ultrasound Med. Biol.*, **37**, 1838–1852.

765

766

767

Arvanitis, C. D., Livingstone, M. S., and McDannold, N. (2013). "Combined Ultrasound and MR Imaging to Guide Focused Ultrasound Therapies in the Brain," *Phys. Med. Biol.*, **58**, 4749–4761.

768

769

770

Chitnis, P. V., Farny, C., and Roy, R. A. (2015). "Singular value decomposition: A better way to analyze cavitation-noise data," *J. Acoust. Soc. Am.*, **137**, 2253–2253.

771

772

773

Choi, J. J., Carlisle, R. C., Coviello, C., Seymour, L., and Coussios, C.-C. (2014). "Non-invasive and real-time passive acoustic mapping of ultrasound-mediated drug delivery," *Phys. Med. Biol.*, **59**, 4861.

774

775

776

Choi, J. J., and Coussios, C.-C. (2012). "Spatiotemporal evolution of cavitation dynamics exhibited by flowing microbubbles during ultrasound exposure," *J. Acoust. Soc. Am.*, **132**, 3538–3549.

- 777 Coussios, C. C., Farny, C. H., Ter Haar, G., and Roy, R. A. (2007). "Role of acoustic  
778 cavitation in the delivery and monitoring of cancer treatment by high-intensity  
779 focused ultrasound (HIFU)," *Int. J. Hyperthermia*, **23**, 105–120.
- 780 Coussios, C. C., and Roy, R. A. (2008). "Applications of Acoustics and Cavitation to  
781 Noninvasive Therapy and Drug Delivery," *Annu. Rev. Fluid Mech.*, **40**, 395–  
782 420.
- 783 Coviello, C., Kozick, R., Choi, J., Gyöngy, M., Jensen, C., Smith, P. P., and Coussios,  
784 C.-C. (2015). "Passive acoustic mapping utilizing optimal beamforming in  
785 ultrasound therapy monitoring," *J. Acoust. Soc. Am.*, **137**, 2573–2585.
- 786 Graham, S.J., Chen, L., Leitch, M., Peters, R.D., Bronskill, M.J., Foster, F.S.,  
787 Henkelman, R.M., and Plewes, D.B. (1999). "Quantifying tissue damage due  
788 to focused ultrasound heating observed by MRI," *Magn. Reson. Med.*, **41**,  
789 321–328.
- 790 Gyongy, M., and Coussios, C.-C. (2010). "Passive Spatial Mapping of Inertial  
791 Cavitation During HIFU Exposure," *IEEE Trans. Biomed. Eng.*, **57**, 48–56.
- 792 Gyöngy, M., and Coussios, C.-C. (2010). "Passive cavitation mapping for localization  
793 and tracking of bubble dynamics," *J. Acoust. Soc. Am.*, **128**, EL175–EL180.
- 794 ter Haar, G. (2007). "Therapeutic applications of ultrasound," *Prog. Biophys. Mol.*  
795 *Biol.*, **93**, 111–129.
- 796 ter Haar, G., and Coussios, C. (2007). "High Intensity Focused Ultrasound: Past,  
797 present and future," *Int. J. Hyperthermia*, **23**, 85–87.
- 798 ter Haar, G., and Coussios, C. (2007). "High intensity focused ultrasound: Physical  
799 principles and devices," *Int. J. Hyperthermia*, **23**, 89–104.
- 800 Hamilton, M. F., and Blackstock, D. T. (1998). *Nonlinear Acoustics*, Academic Press,



- 801 Haqshenas, S. R., and Saffari, N. (2015). “Multi-resolution analysis of passive  
802 cavitation detector signals,” J. Phys. Conf. Ser., **581**, 012004.
- 803 Haworth, K. J., Mast, T. D., Radhakrishnan, K., Burgess, M. T., Kopechek, J. A.,  
804 Huang, S. L., McPherson, D. D., and Holland C. K. (2012). “Passive imaging  
805 with pulsed ultrasound insonations,” J. Acoust. Soc. Am., **132**, 544–553.
- 806 Jensen, C. R., Cleveland, R. O., and Coussios, C. C. (2013). “Real-time temperature  
807 estimation and monitoring of HIFU ablation through a combined modeling  
808 and passive acoustic mapping approach,” Phys. Med. Biol., **58**, 5833.
- 809 Jensen, C. R., Ritchie, R. W., Gyöngy, M., Collin, J. R. T., Leslie, T., and Coussios,  
810 C.-C. (2012). “Spatiotemporal monitoring of high-intensity focused ultrasound  
811 therapy with passive acoustic mapping,” Radiology, **262**, 252–261.
- 812 Jones, R. M., O’Reilly, M. A., and Hynynen, K. (2013). “Transcranial passive  
813 acoustic mapping with hemispherical sparse arrays using CT-based skull-  
814 specific aberration corrections: a simulation study,” Phys. Med. Biol., **58**,  
815 4981.
- 816 Khokhlova, V. A., Bailey, M. R., Reed, J. A., Cunitz, B. W., Kaczkowski, P. J., and  
817 Crum, L. A. (2006). “Effects of nonlinear propagation, cavitation, and boiling  
818 in lesion formation by high intensity focused ultrasound in a gel phantom,” J.  
819 Acoust. Soc. Am., **119**, 1834–1848.
- 820 Khokhlova, V. A., Fowlkes, J. B., Roberts, W. W., Schade, G. R., Xu, Z., Khokhlova,  
821 T. D., Hall, T. L., Maxwell A. D., Wang Y-N, and Cain C. A. (2015).  
822 “Histotripsy methods in mechanical disintegration of tissue: Towards clinical  
823 applications,” Int. J. Hyperthermia, **31**, 145–162.

- 824 <sup>a</sup>Kwan, J. J., Graham, S., Myers, R., Carlisle, R., Stride, E., and Coussios, C. C.  
 825 (2015). "Ultrasound-induced inertial cavitation from gas-stabilizing  
 826 nanoparticles," *Phys. Rev. E*, **92**, 023019.
- 827 <sup>b</sup>Kwan, J. J., Myers, R., Coviello, C. M., Graham, S. M., Shah, A. R., Stride, E.,  
 828 Carlisle, R. C., and Coussios, C. C. (2015). "Ultrasound-Propelled Nanocups  
 829 for Drug Delivery," *Small*.
- 830 Lake, D. (1999). "Efficient Maximum Likelihood Estimation for Multiple and  
 831 Coupled Harmonics," ARL-TR-2014,
- 832 Liang, H.-D., Tang, J., and Halliwell, M. (2010). "Sonoporation, drug delivery, and  
 833 gene therapy," *Proc. Inst. Mech. Eng. [H]*, **224**, 343–361.
- 834 McDannold, N., Vykhodtseva, N., and Hynynen, K. (2008). "Blood-Brain Barrier  
 835 Disruption Induced by Focused Ultrasound and Circulating Preformed  
 836 Microbubbles Appears to Be Characterized by the Mechanical Index,"  
 837 *Ultrasound Med. Biol.*, **34**, 834–840.
- 838 Mo, S., Coussios, C.-C., Seymour, L., and Carlisle, R. (2012). "Ultrasound-enhanced  
 839 drug delivery for cancer," *Expert Opin. Drug Deliv.*, **9**, 1525–1538.
- 840 Muir, T. G., and Carstensen, E. L. (1980). "Prediction of nonlinear acoustic effects at  
 841 biomedical frequencies and intensities," *Ultrasound Med. Biol.*, **6**, 345–357.
- 842 Myung, I. J. (2003). "Tutorial on maximum likelihood estimation," *J. Math. Psychol.*,  
 843 **47**, 90–100.
- 844 O'Reilly MA, Hynynen K. (2012). "Blood-Brain Barrier: Real-time Feedback-  
 845 controlled Focused Ultrasound Disruption by Using an Acoustic Emissions-  
 846 based Controller," *Radiology* 263: 96–106.

- 847 O'Reilly, M. A., Jones, R. M., and Hynynen, K. (2014). "Three-Dimensional  
848 Transcranial Ultrasound Imaging of Microbubble Clouds Using a Sparse  
849 Hemispherical Array," IEEE Trans. Biomed. Eng., **61**, 1285–1294.
- 850 Quesson, B., Laurent, C., Maclair, G., de Senneville, B. D., Mougnot, C., Ries, M.,  
851 Carteret, T., Rullier, A., and Moonen, C. T. W. (2011). "Real-time volumetric  
852 MRI thermometry of focused ultrasound ablation in vivo: a feasibility study in  
853 pig liver and kidney," NMR Biomed., **24**, 145–153.
- 854 Quesson, B., de Zwart, J. A., and Moonen, C. T. W. (2000). "Magnetic resonance  
855 temperature imaging for guidance of thermotherapy," J. Magn. Reson.  
856 Imaging, **12**, 525–533.
- 857 Rabkin, B. A., Zderic, V., Crum, L. A., and Vaezy, S. (2006). "Biological and  
858 physical mechanisms of HIFU-induced hyperecho in ultrasound images,"  
859 Ultrasound Med. Biol., **32**, 1721–1729.
- 860 Rabkin, B. A., Zderic, V., and Vaezy, S. (2005). "Hyperecho in ultrasound images of  
861 HIFU therapy: Involvement of cavitation," Ultrasound Med. Biol., **31**, 947–  
862 956
- 863 Rifai, B., Arvanitis, C. D., Bazan-Peregrino, M., and Coussios, C.-C. (2010).  
864 "Cavitation-enhanced delivery of macromolecules into an obstructed vessel,"  
865 J. Acoust. Soc. Am., **128**, EL310–EL315.
- 866 Salgaonkar VA, Datta S, Holland CK, Mast TD. (2009). "Passive cavitation imaging  
867 with ultrasound arrays," J Acoust Soc Am 2009;126(6):3071–3083.
- 868 de Senneville, B. D. de, Mougnot, C., Quesson, B., Dragonu, I., Grenier, N., and  
869 Moonen, C. T. W. (2007). "MR thermometry for monitoring tumor ablation,"  
870 Eur. Radiol., **17**, 2401–2410.

- 871 Whipps, G. (2003). *Coupled harmonics : estimation and detection* The Ohio State  
872 University. Retrieved from  
873 [https://etd.ohiolink.edu/ap/10?0::NO:10:P10\\_ACCESSION\\_NUM:osu126131](https://etd.ohiolink.edu/ap/10?0::NO:10:P10_ACCESSION_NUM:osu126131)  
874 8405  
875
- 876 Yu, T., and Xu, C. (2008). "Hyperecho as the Indicator of Tissue Necrosis During  
877 Microbubble-Assisted High Intensity Focused Ultrasound: Sensitivity,  
878 Specificity and Predictive Value," *Ultrasound Med. Biol.*, **34**, 1343–1347.
- 879 Zivanovic, M. and Gonzalez-Izal, M.,(2012) "Nonstationary harmonic modeling for  
880 ECG removal in surface EMG signals", *IEEE Trans. Biomed. Eng.*, **59**, 1633-  
881 1640.

882